Microporous and Mesoporous Materials 399 (2026) 113859

Contents lists available at ScienceDirect

Microporous and Mesoporous Materials

journal homepage: www.elsevier.com/locate/micromeso

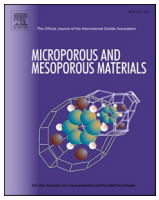

Thermal desorption kinetics and framework evolution in VOC-loaded FAU-Type zeolite Y: An *in situ* XRPD study

Maura Mancinelli [a,*], Matteo Ardit [b], Luisa Pasti [c], Tatiana Chenet [c], Carlotta Giacobbe [d], Annalisa Martucci [a,**]

[a] Department of Physics and Earth Sciences, University of Ferrara, Via Saragat 1, I-44121, Ferrara, Italy
[b] Department of Geosciences, University of Padova, Via Gradenigo 6, I-35131, Ferrara, Italy
[c] Department of Environmental and Prevention Sciences, University of Ferrara, via Borsari 46, I-44121, Ferrara, Italy
[d] European Synchrotron Radiation Facility, 71 avenue des Martyrs, 38000, Grenoble, France

ARTICLE INFO

Keywords:
Toluene
Chlorobenzene
Zeolite
Adsorption
Desorption
XRPD

ABSTRACT

This study reports a detailed investigation of the desorption kinetics of toluene and chlorobenzene from a high-silica FAU-type Y zeolite ($SiO_2/Al_2O_3 \approx 200$) by *in situ* synchrotron X-ray powder diffraction under dynamic (298–973 K) and isothermal (443–523 K) conditions. Dynamic XRPD data reveal a progressive unit cell contraction (~0.4–0.5 %) and an increase in the intensity of the (111) reflection, consistent with the gradual release of VOCs and pore evacuation. Activation energies were calculated using Avrami–Erofeev and Arcenegui–Troya kinetic models, the latter incorporating non-Arrhenius behavior attributed to cooperative effects. The higher activation energy observed for chlorobenzene (28.13 ± 3.93 kJ/mol) compared to toluene (17.31 ± 0.66 kJ/mol) is attributed to stronger quadrupole–cation interactions, reduced rotational entropy, and cooperative desorption barriers arising from molecular crowding. These findings provide fundamental structural insights into host–guest interactions and framework stability during VOC desorption, informing the design of regenerable zeolite adsorbents for environmental applications.

1. Introduction

The increasing prevalence of toluene and chlorobenzene in aquatic environments, driven by industrial discharge, petroleum refining, and improper waste disposal, has raised serious environmental and public health concerns. To mitigate associated risks, the U.S. Environmental Protection Agency (EPA) has established Maximum Contaminant Levels (MCLs) of 1 mg/L for toluene and 0.1 mg/L for chlorobenzene [1]. Exceeding these thresholds can result in adverse health effects, including neurotoxicity and organ damage, highlighting the urgent need for efficient and selective removal strategies [2,3].

Zeolites are crystalline microporous aluminosilicates extensively used in catalysis, adsorption, and ion exchange owing to their high specific surface area, thermal stability, and well-defined pore architecture. Their distinctive physicochemical properties including hydrophobicity, structural stability, and tunable pore dimensions make them particularly effective in advanced pollution control technologies, targeting complex contaminant mixtures in groundwater systems. Among the available zeolites, FAU-type Y zeolite has emerged as an auspicious material due to its large pore apertures, high chemical stability, cost-efficiency, and effectiveness in groundwater remediation and water purification systems [4–7]. Notably, Y zeolite has shown excellent adsorption capabilities for toluene and chlorobenzene from aqueous media in both single- and multi-component conditions [8].

A key advantage of zeolites in environmental applications lies in their ability to undergo regeneration and reuse, typically through controlled thermal treatments [9–13]. In the context of volatile organic compound removal, particularly for aromatic hydrocarbons such as toluene and chlorobenzene, thermal desorption must be carefully managed to preserve the crystallinity and adsorptive functionality of the zeolite. Indeed, thermal regeneration can lead to structural modifications analogous to those observed upon dehydration, including unit cell variations, distortions in T–O–T bond angles (T = Si or Al), breaking of Si–O or Al–O bonds, and in some cases, partial amorphization or irreversible framework collapse [14–18]. These structural changes can reduce pore accessibility, modify the distribution and chemical nature of

* Corresponding author.
** Corresponding author.
E-mail addresses: maura.mancinelli@unife.it (M. Mancinelli), mrs@unife.it (A. Martucci).

https://doi.org/10.1016/j.micromeso.2025.113859
Received 20 July 2025; Received in revised form 29 August 2025; Accepted 10 September 2025
Available online 11 September 2025
1387-1811/© 2025 The Authors. Published by Elsevier Inc. This is an open access article under the CC BY-NC-ND license (http://creativecommons.org/licenses/by-nc-nd/4.0/).

active sites, and ultimately affect the zeolite's adsorption or catalytic performance. Consequently, understanding the response to heating of zeolites is crucial for ensuring long-term effectiveness in pollutant removal applications.

For this purpose, *in situ* techniques, such as temperature- and time-resolved synchrotron X-ray powder diffraction (XRPD), offer powerful tools for real-time monitoring of structural evolution under thermal treatment [19–26]. These methods enable direct observation of framework dynamics, including progressive changes in lattice parameters, distortions of T–O–T bond angles, and potential phase transitions, thereby providing critical insights into the thermal response and regeneration capacity of zeolitic materials. In this context, kinetic analysis is essential for interpreting thermally induced desorption and the resulting structural transformations. Desorption processes are governed by activation energies, which quantify the energy required for molecular release and framework reorganization. Activation energies are highly sensitive to various parameters, including the physicochemical properties of the adsorbed species, the Si/Al ratio of the framework, pore topology, and the nature and distribution of extra-framework cations. Furthermore, the kinetic behavior may evolve during desorption due to changes in diffusion pathways or progressive structural degradation.

Over the past decades, different kinetic model-free isoconversional approaches have been developed to evaluate activation energies without assuming a predefined reaction mechanism [27–34]. Despite their proven utility in broader materials science and thermal analysis, these approaches remain less exploited in zeolite research, particularly in the context of real-time investigations of organic molecules desorption under thermal stress.

In this study, we examine the thermal desorption kinetics of toluene and chlorobenzene from FAU-type Y zeolite using synchrotron X-ray diffraction data collected in both variable-temperature (298–973 K) and isothermal (443, 463, 483, and 523 K) conditions to assess structural transformations alongside kinetic parameters. *In situ* isothermal XRPD enables time-resolved monitoring of structural changes at selected temperatures, unit cell dimensional variations, and the evolution of Bragg reflection intensities associated with desorption events and framework distortions. By tracking the time-dependent behavior of selected diffraction peaks, typically via integrated intensity or peak area, reaction progress curves can be constructed and analyzed using model-free isoconversional methods (e.g., Friedman, Vyazovkin) [35–37] to extract apparent activation energies without assuming specific kinetic models.

This methodology offers several key advantages: it provides direct crystallographic evidence of structural dynamics, decouples molecular desorption from concurrent framework modifications, and captures transient intermediate states not observable in conventional non-isothermal experiments. XRPD simultaneously reveals microscopic structural evolution, allowing for direct correlation between molecular release events and framework alterations. This integrated analysis facilitates the identification of critical thermal thresholds beyond which regeneration efficiency and structural integrity are compromised.

Finally, this combined *in situ* approach allows us to link desorption kinetics with framework behavior, providing a mechanistic understanding of regeneration processes in FAU-type zeolites. These insights are essential for the rational design of thermally robust adsorbents for environmental remediation and volatile organic compound abatement.

2. Experimental

The zeolite selected for this study was a hydrophobic FAU-type Y zeolite (HSZ-390HUA, Tosoh Corporation) in its protonic (H^+) form. The material exhibited a high degree of dealumination, as indicated by a SiO_2/Al_2O_3 molar ratio of approximately 200 and contained only 0.05 mass% Na_2O. Structurally, the FAU framework is composed of cuboctahedral sodalite cages (β-cages) connected through double six-membered rings (D6Rs) at four of the six-membered ring faces, forming large supercages (α-cages) approximately 1.2 nm in diameter. These cavities are accessible via 12-membered ring windows with a free aperture of ~0.74 nm, enabling the adsorption of relatively large organic molecules.

The textural properties of the zeolite were investigated by nitrogen physisorption at 77 K (liquid nitrogen temperature), using an Autosorb-1-MP volumetric analyzer (Quantachrome Instruments). Measurements were performed over a pressure range of 5×10^{-6} to 760 Torr. Before analysis, the sample was degassed under high vacuum to eliminate physisorbed contaminants. The activation protocol consisted of a three-step heating sequence: 1 h at 363 K, 1 h at 403 K, and 16 h at 573 K, reaching a final pressure of 1×10^{-9} Torr.

The specific surface area was calculated using the Brunauer–Emmett–Teller (BET) method, applying a maximum relative pressure (P/P_0) of 0.01. Pore size distribution was derived from the desorption branch of the isotherm using the Non-Local Density Functional Theory (NLDFT) model, assuming cylindrical pore geometry.

The zeolite displayed a high total surface area of 853 m^2/g, with 616 m^2/g attributable to its microporous structure. The material featured characteristic 1.2 nm micropores, contributing a pore volume of 0.21 cm^3/g. In addition, two families of mesopores were identified: pores centered at 2.2 nm and 5 nm, with respective pore volumes of 0.12 cm^3/g and 0.08 cm^3/g. The total pore volume of the sample was 0.62 cm^3/g. [38,39]. The textural properties are summarized in Table S1.

Toluene – purity 99.9 % and Chlorobenzene – purity 99.8 % were purchased from Merck (Darmstadt, Germany). The water was Milli-Q grade (Millipore, Ma, USA).

To prepare Y zeolite saturated with Toluene (TOL) and Chlorobenzene (ClB), denoted as Y-TOL and Y-ClB respectively, 100 mg of Y zeolite were brought into contact with 100 mL of an aqueous solution containing TOL and ClB at a concentration of 200 ppm, in sealed flasks. Under these conditions, the saturation capacity of the Y zeolite for both TOL and ClB has already been established [8]. The suspension was maintained at 25.3 ± 0.5 °C for 24 h under continuous stirring. The solid samples were then separated from the aqueous phase by centrifugation at 14,000 rpm for 30 min, thoroughly washed with deionized water, and dried at 40 °C overnight.

Non-isothermal thermogravimetric analyses were carried out in air up to 1090 K using a Netzsch STA 409 PC LUXX® simultaneous TG/DTA analyzer, with a heating rate of 10 K/min (Fig. S1).

In situ time-resolved X-ray powder diffraction (XRPD) measurements were performed at the ID22 beamline of the European Synchrotron Radiation Facility (ESRF, Grenoble) in high-resolution mode. Diffraction data were acquired at a wavelength of 0.0400031 nm, employing a transfocator equipped with compound refractive lenses to attenuate third-order and higher-order harmonics. The zeolite samples, packed into an open-ended 0.7 mm quartz capillary, were heated from room temperature to 973 K using a hot air blower. Diffracted X-rays were recorded every 20 K simultaneously by nine detectors, with a heating rate of 0.083 K/s in the 0.4–24.5° 2θ range. Fig. 1 illustrates the evolution of the Y-type zeolites loaded with toluene (Fig. 1a) and chlorobenzene (Fig. 1b), particularly in the low-angle region (1.0–6.0° 2θ), highlighting the structural transformations associated with their thermal desorption.

Four isothermal XRPD measurements were then performed at temperatures of 443, 463, 483, and 523 K, which were selected based on significant features observed in the DTG and DTA profiles. Each pattern was individually refined using the Rietveld method, implemented via the EXPGUI interface for the GSAS software package. The diffraction data were refined in the cubic *Fd*−3 space group, starting from the structural models reported by Chenet et al. [28] and Pasti et al. [8] for Y-CB and Y-Tol, respectively.

Refined parameters included the scale factor for all datasets, fractional atomic coordinates, occupancy values of extra-framework constituents, and isotropic atomic displacement parameters (ADPs). To

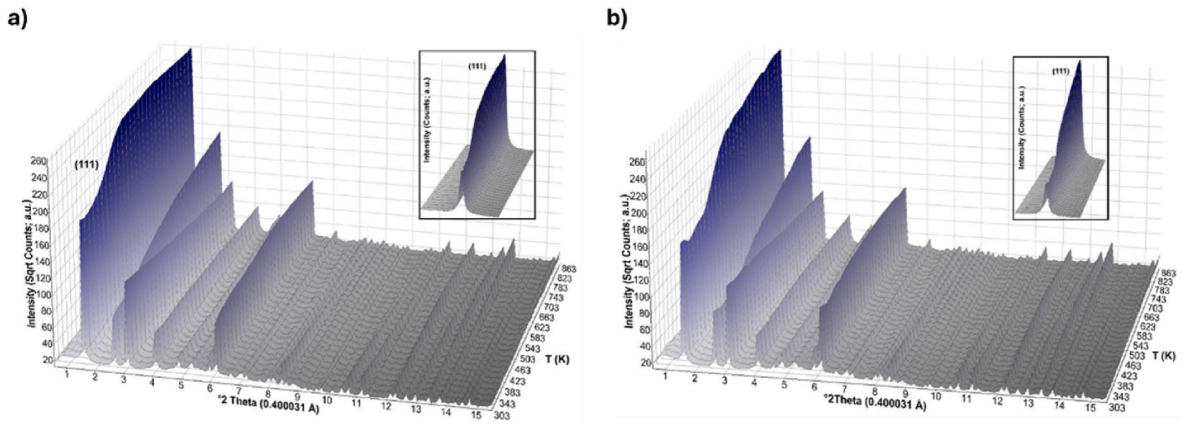

Fig. 1. XRD patterns and focus on low-angle region showing the structural evolution of Y-type zeolites loaded with (a) toluene and (b) chlorobenzene during thermal desorption.

minimize the number of refined variables, ADPs were constrained for atoms of the same type (e.g., Si and O). Soft constraints were applied to Si–O bond lengths (0.16 ± 0.004 nm) during early refinement stages and later released. The Bragg peak profiles were fitted using a modified pseudo-Voigt function (with a 0.01 % cut-off), while background contributions were modelled with a 16-coefficient Chebyshev polynomial.

Kinetic analysis of the isothermal data was carried out following the method proposed by Hancock and Sharp [40].

3. Results and discussion

3.1. Analysis of variable-temperature data from in situ XRPD and TGA data

Rietveld refinements of the room-temperature XRPD data confirmed the cubic *Fd*-3 symmetry for both Y-TOL and Y-ClB samples, in agreement with that of the initial structural models. Both the organic guest molecules were located within the supercages, statistically distributed on six equivalent orientations resulting from the 6-fold axis parallel to [111].

Upon heating from 303.15 K to 863.15 K, no evidence of phase transition or symmetry change was observed in the patterns. Notably, there is a significant increase in intensity of the (111) reflection as the temperature rises, which is associated with the gradual decrease in electron density (averaged over the unit cell) resulting from the removal of extra-framework molecules within the channels (Fig. 2). Bragg reflections in the intermediate 2θ region, which can be ascribed to the zeolite framework, display much less variation. Both samples displayed a gradual and continuous contraction of the unit cell, resulting in a total volume shrinkage of approximately 0.46 % for Y-TOL and 0.42 % for Y-ClB.

Fig. 3 shows that the desorption of organic molecules by HSZ-Y zeolite varies by molecule type. To quantify the number of guest molecules (toluene and chlorobenzene) per unit cell, Rietveld refinement was performed using GSAS. The number of molecules per unit cell (Z) is determined as the sum over all crystallographic sites associated with the guest molecule, according to formula (1):

$$Z = \sum (multiplicity\ x\ occupancy) \quad (1)$$

Here, *multiplicity* corresponds to the number of symmetry-equivalent positions in the unit cell, and *occupancy* represents the fraction of the site occupied by the molecule. Each site is defined in GSAS with atomic coordinates, occupancy, and symmetry; the software automatically applies the appropriate multiplicity. The total number of molecules per unit cell is obtained by summing the contributions from all relevant

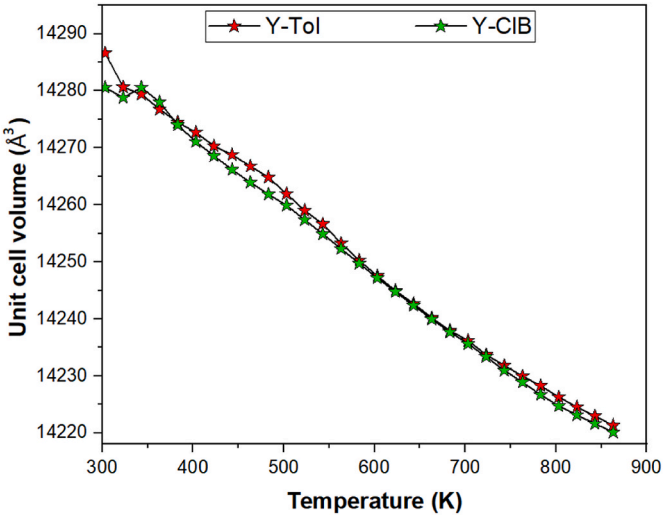

Fig. 2. Variations in unit cell parameters of Y-type zeolites loaded with toluene (Y-tol) and chlorobenzene (Y-clb) during heating.

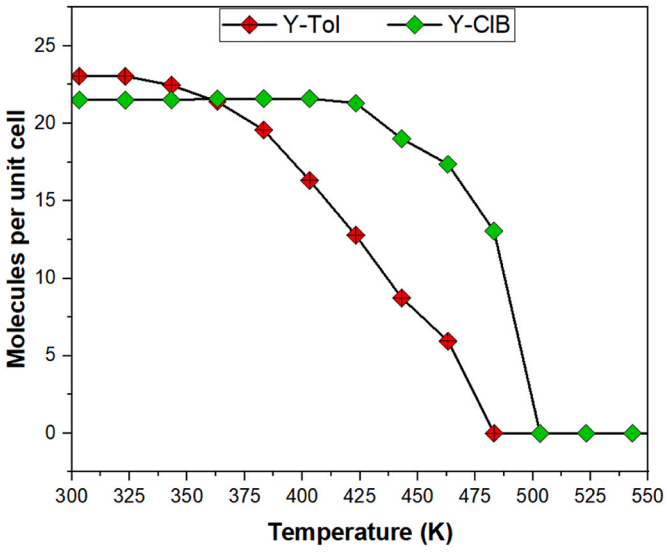

Fig. 3. Desorption behavior of organic molecules from HSZ-Y zeolite as a function of molecule type with toluene (Y-tol) and chlorobenzene (Y-clb). The number of molecules per unit cell was determined by Rietveld refinement using GSAS, based on site occupancy and symmetry-derived multiplicity.

sites.

Toluene desorbs gradually over a wide temperature range (from room temperature to about 480 K), whereas chlorobenzene is firmly retained in the extraframework sites of the zeolite up to 425 K and desorbs rapidly within a 75 K thermal range (i.e., at about 500 K). These different desorption behaviors are reflected in variations in the inter-tetrahedral bond angles of the zeolite that depends on the type of organic molecule adsorbed prior to heat treatment.

In Y-TOL, desorption was nearly complete at around 483 K, accompanied by slight modifications in the T-O-T angles (Fig. 4). Specifically, the T1–O1–T2 and T1–O4–T2 angles shifted from approximately 138° and 144° at 303 K to about 140° and 138° in the 543–563 K range respectively. These changes indicate a cooperative relaxation of the framework as the guest molecules are expelled, reflecting the release of internal strain created by host–guest interactions.

For Y-ClB, in the 303–503 K temperature range, the T–O–T angles remained relatively stable, with T1–O1–T2 ranging from 133° to 135° and T1–O4–T2 from 153° to 154°. This result suggests that the framework remained in a strained configuration due to the continued presence of ClB. Angular modifications became noticeable only above 523 K, when the complete ClB desorption occurred, with values converging towards those observed for fully desorbed Y-TOL (approximately 140° and 138° at 563–583 K).

The distinct desorption dynamics and associated structural responses can be attributed to differences in host–guest interactions. The electron-withdrawing chlorine in ClB enhances quadrupole–cation electrostatics and dispersion interactions with the zeolite walls, stabilizing the guest and delaying desorption and framework relaxation. In contrast, the weaker interactions of TOL result in earlier desorption and a more immediate elastic response of the framework. These findings were also confirmed by the kinetic data discussed in the next section.

3.2. *Kinetic analysis of toluene and chlorobenzene desorption from zeolite Y*

To determine the activation energy (Ea) of the structural transformation occurring during thermal treatment, a kinetic analysis was conducted using X-ray diffraction data collected under isothermal conditions. The kinetic curves were evaluated using the classical Avrami–Erofeev model for heterogeneous solid-state reactions (Strømme, 1986) [41]:

$$\alpha = 1 - \exp\{-[(-kt)^n]\} \quad (2)$$

where α is the fraction of transformed material as a function of time, and k and n are constants derived from the model.

The evolution of the intensity and integrated area of the (111) Bragg reflection, associated with the extraframework content of the zeolite (see previous section), was monitored over time at 443, 463, 483, and 523 K (Fig. 5). The integrated peak area is generally more reliable for quantitative kinetic analysis than the maximum peak intensity, as it accounts for the entire peak profile and is less affected by noise and instrumental fluctuations. Maximum peak intensity, while quicker to obtain, is more susceptible to noise and may underestimate subtle changes in structure. Normalization of intensity (I/I_0) facilitates comparisons but only reflects the peak maximum, missing the full extent of transformation. Thus, the integrated area is preferred for accurate kinetic modelling, while normalized intensity can provide qualitative insights [42,43].

Assuming a first-order kinetic model, the time evolution of the normalized intensity $I(t)/I_0$ can be described as:

$$I(t) = I_0 e^{-kt} \quad (3)$$

where $I(t)$ is the intensity (or area) at time t, I_0 is the initial value, and k is the apparent rate constant at the given temperature. For each isothermal treatment, the rate constant k was obtained by nonlinear least-squares fitting of the experimental data to the above equation.

The natural logarithm of the rate constants was then plotted using the Arrhenius plot:

$$\ln k = \ln A - \frac{Ea}{RT} \quad (4)$$

where:

- Ea is the apparent activation energy (J mol^{-1}),
- A is the pre-exponential factor,
- R is the universal gas constant (8.314 J mol^{-1} K^{-1}).

This model produces a linear plot of ln k versus 1/T, with the slope equal to −Ea/R (Fig. 6).

Despite being similarly located in the central supercage and having comparable orientational freedom within the Y-zeolite framework, chlorobenzene consistently exhibits a higher apparent activation energy compared to toluene, as evidenced by the values of 28.13 ± 3.93 kJ/mol versus 17.31 ± 0.66 kJ/mol (A/A_0 data) (Table 1).

This difference can be rationalized by a combination of physicochemical factors. Firstly, the electron-withdrawing chlorine substituent in chlorobenzene increases the ring's quadrupole moment, thereby strengthening quadrupole–cation interactions with the extra-framework protons of the zeolite [44]. Secondly, chlorobenzene's greater vibrational polarizability [45] enhances London dispersion forces, intensifying van der Waals interactions with the zeolite pore walls. Additionally, toluene benefits from rotational entropy contributions due

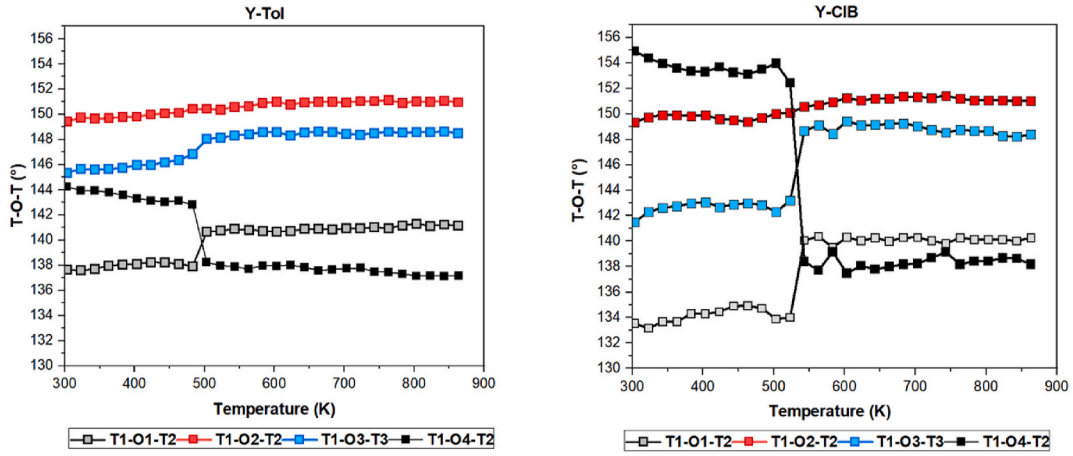

Fig. 4. Evolution of T–O–T bond angles in Y-toluene (Y-tol) and Y-chlorobenzene (Y-clb) loaded zeolites as a function of temperature.

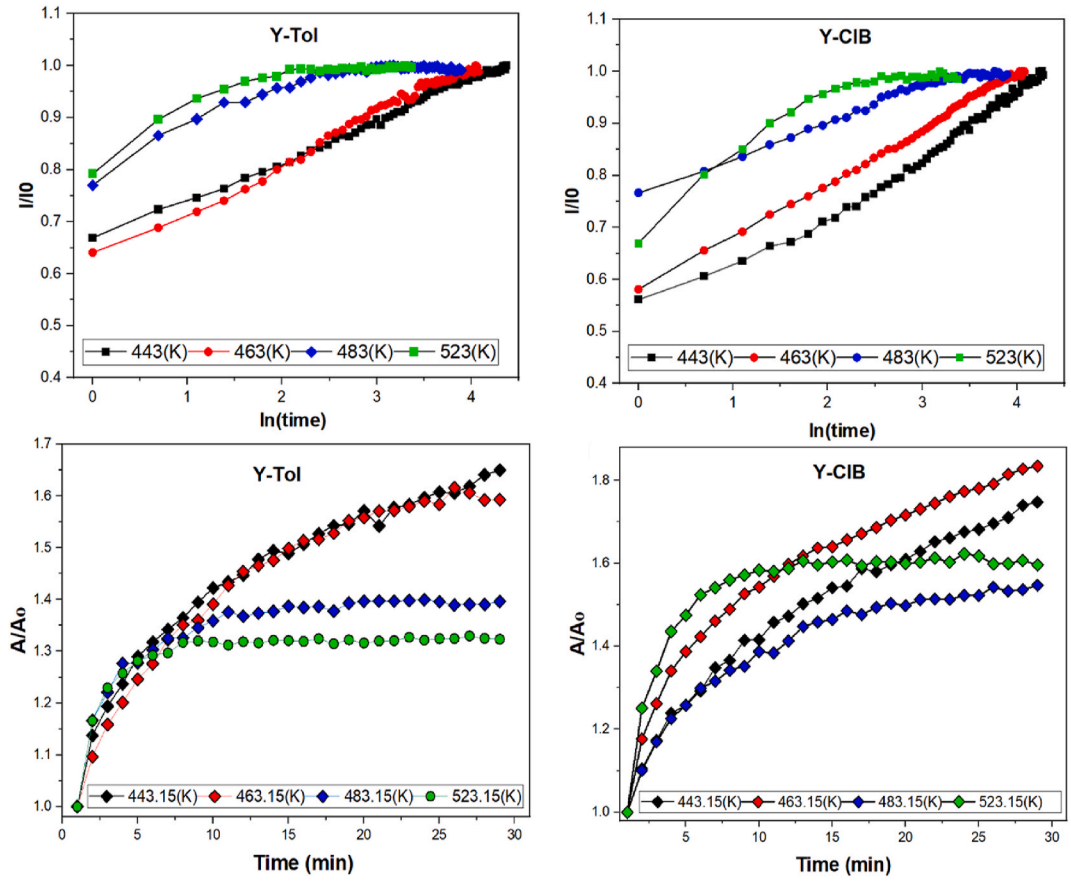

Fig. 5. Evolution of the intensity and integrated area of the (111) Bragg reflection for Y-toluene (Y-tol) and Y-chlorobenzene (Y-clb) samples during isothermal treatments at 443, 463, 483, and 523 K.

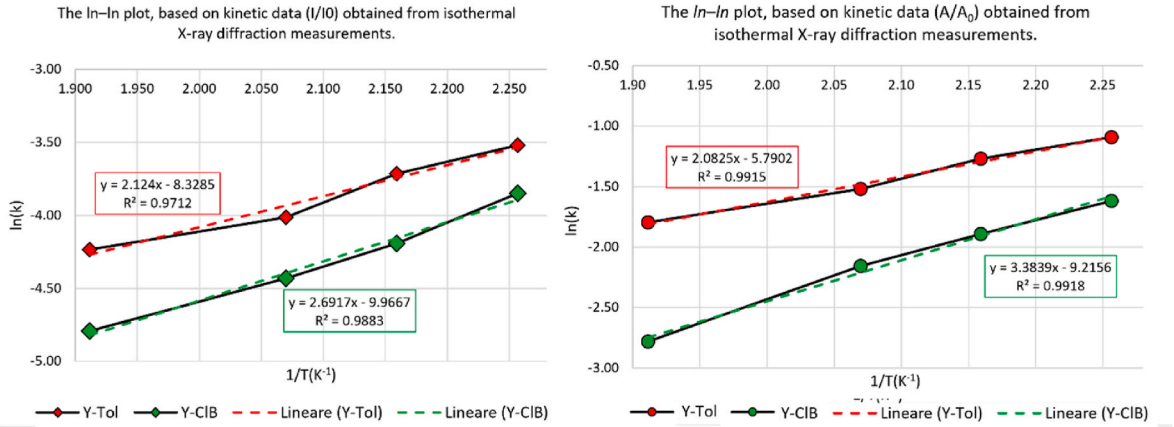

Fig. 6. Plots for the desorption process in Y-toluene (Y-tol) and Y-chlorobenzene (Y-clb) samples, showing the linear relationship between ln k and 1/T.

to methyl rotor modes that persist into the transition state, which effectively lowers its activation energy through a more favorable entropy of activation (ΔS±) [46]. The zero-point energy difference is also higher for chlorobenzene, owing to the elevated vibrational frequencies of the C–Cl bond compared to the C–H bond in toluene, which increases the energy gap between the ground and transition states [47]. Finally, crowding effects may play a role; chlorobenzene desorbs at higher temperatures and remains longer within the pore system, fostering increased molecular interactions and cooperative desorption barriers that contribute to the elevated apparent activation energy [48]. Collectively, these factors offer a coherent explanation for the observed difference in E_a values and highlight the complex interplay between molecular properties and zeolite host–guest dynamics.

However, adsorption and diffusion in porous systems like zeolites are influenced by multiple cooperative effects, including changes in configurational entropy, guest–host interactions, and site accessibility with temperature. For these reasons, the activation energies were also determined by applying the Arcenegui–Troya model [49–51] to the temperature-dependent evolution of the integrated peak areas obtained from isothermal measurements. This model is an improvement of the classical Arrhenius approach because it incorporates a second-order term in 1/T. This term more accurately accounts for deviations from

Table 1
Summary of intensities and derived activation energies for desorption in Y-toluene (Y-tol) and Y-chlorobenzene (Y-clb) zeolite samples.

Y-Tol			Y-ClB		
A/A_0	Value	sd	A/A_0	Value	sd
Intercept	5.79	±0.17	*Intercept*	9.22	±0.13
Slope	2.08	±0.079	*Slope*	3.38	±0.47
Ea=	17.31	±0.66 kJ/mol	*Ea=*	28.13	±3.93 kJ/mol
Equation	*y=2.08-5.79x*		*Equation*	*y=9.22-3.38x*	
R^2*=0.9915*			R^2*=0.9918*		
Y-Tol			**Y-ClB**		
I/I_0	**Value**	**sd**	**I/I_0**	**Value**	**sd**
Intercept	8.33	±0.20	*Intercept*	9.97	±0.19
Slope	2.12	±0.11	*Slope*	2.69	±0.39
E_a*=*	17.66	±0.90 kJ/mol	*Ea=*	22.38	±3.22 kJ/mol
Equation	*y=2.12-8.33x*		*Equation*	*y=9.97-2.69x*	
R^2*=0.9712*			R^2*=0.9883*		

linearity often observed in complex or multi-step systems.

Rate constants (k) were derived from normalized peak areas at the four selected temperatures (443.15 K, 463.15 K, 483.15 K, and 523.15 K) and were fitted using the modified equation:

$$\ln k = a + \frac{b}{T} + \frac{c}{T^2} \tag{5}$$

where a, b, and c are regression coefficients.

From this relationship, the temperature-dependent activation energy was calculated as:

$$Ea\,(T) = -R\left(\frac{d\ln k}{d\left(\frac{1}{T}\right)}\right) = R\left(b + \frac{2c}{T}\right) \tag{6}$$

This expression reveals how E_a evolves with temperature, considering the curvature observed in ln k vs. 1/T plots and reflecting multi-step or diffusion-limited processes. For toluene, the fitting returned: a = 4.14, b = 1.62 × 103, c = −8.54 × 105, resulting in an E_a that decreases from ~18.5 kJ/mol at 443 K to ~13.6 kJ/mol at 523 K. This inverse temperature dependence suggests a transition from a kinetically controlled adsorption or reaction step to a regime dominated by diffusion or desorption processes, facilitated at higher temperatures by increased molecular mobility and reduced adsorbate-zeolite interaction strength.

In contrast, chlorobenzene displayed the opposite behavior, with: a = 21.25, b = −1.42 × 104, c = 2.77 × 106 giving activation energies increasing from ~14.2 kJ/mol at 443 K to ~30.1 kJ/mol at 523 K. This trend may be indicative of a more energy-intensive steps such as rearrangement within the pore structure or disruption of strong adsorbate-framework interactions, which become more dominant at higher temperatures. The increase in E_a may also reflect activation of higher-energy adsorption sites or pore accessibility limitations caused by thermal effects on the zeolite framework.

The contrasting trends for toluene and chlorobenzene point to fundamentally different mechanistic regimes. Toluene likely undergoes a shift toward transport-limited behavior, whereas chlorobenzene exhibits temperature-activated processes that suggest stronger framework interactions or multi-step kinetics.

Overall, the Arcenegui–Troya model proves essential for accurately describing the non-linear temperature dependence of reaction kinetics in zeolite-based systems. By using a second-order dependence on 1/T, this model reveals mechanistic features that are hidden under the assumption of linear Arrhenius behavior and supports a more nuanced interpretation of adsorbate–framework interactions in thermal processes.

4. Conclusions

This study investigates the thermal desorption of toluene and chlorobenzene from high silica Y-zeolites using *in situ* synchrotron XRPD and model-free kinetic modeling. Despite both compounds being situated within the supercage and demonstrating comparable freedom of orientation, they display distinct desorption behaviors. Toluene gradually desorbs at approximately 443 K, suggesting weaker interactions with the zeolite framework. Conversely, chlorobenzene remains retained until around 523 K, attributed to stronger stabilization through π-π interactions and its larger quadrupole moment.

The increase in the (111) reflection intensity with heating, along with alterations in T–O–T bond angles, indicates that framework relaxation for toluene occurs earlier and more gradually. In contrast, chlorobenzene shows sharper angular changes only at elevated temperatures.

Notwithstanding the existence of local distortions, the unit cell volume remains nearly constant, suggesting that structural relaxation occurs without a notable contraction of the framework. The kinetic analysis corroborates these findings, revealing that chlorobenzene possesses a higher apparent activation energy (28.13 ± 3.93 kJ/mol) in comparison to toluene (17.31 ± 0.66 kJ/mol), indicating stronger guest–host interactions. The application of the Arcenegui–Troya model demonstrates that the activation energy for toluene decreases from approximately 18.5 to 13.6 kJ/mol between 443 and 523 K, which aligns with a transition to diffusion-limited desorption. On the contrary, chlorobenzene displays high and relatively stable energy barriers, implying a kinetically constrained release mechanism.

In conclusion, the relationship between desorption behavior and framework evolution in FAU-type zeolites is profoundly affected by the nature of the guest molecules.

The integration of structural and kinetic data offers significant insights for the rational design of zeolitic materials intended for selective VOC removal and thermally efficient regeneration.

CRediT authorship contribution statement

Maura Mancinelli: Writing – original draft, Methodology, Investigation, Formal analysis, Data curation. **Matteo Ardit:** Investigation, Data curation, Conceptualization. **Luisa Pasti:** Formal analysis. **Tatiana Chenet:** Formal analysis. **Carlotta Giacobbe:** Formal analysis. **Annalisa Martucci:** Visualization, Supervision, Conceptualization.

Declaration of competing interest

The authors declare the following financial interests/personal relationships which may be considered as potential competing interestsMartucci Annalisa reports financial support was provided by National Recovery and Resilience Plan (NRRP), Mission 04 Component 2 Investment 1.5 – NextGenerationEU, Call for tender n. 3277 dated December 30, 2021, Award Number: 0001052 dated June 23, 2022. If there are other authors, they declare that they have no known competing financial interests or personal relationships that could have appeared to influence the work reported in this paper.

Acknowledgements

Project funded under the National Recovery and Resilience Plan (NRRP), Mission 04 Component 2 Investment 1.5 – NextGenerationEU, Call for tender n. 3277 dated December 30, 2021, Award Number: 0001052 dated June 23, 2022.

Appendix A. Supplementary data

Supplementary data to this article can be found online at https://doi.org/10.1016/j.micromeso.2025.113859.

Data availability

Data will be made available on request.

References

[1] U.S. Environmental Protection Agency (EPA), National primary drinking water standards. www.epa.gov/safewater, 2003. (Accessed 17 July 2025).

[2] X. Li, Y. Chang, Z. Li, C. Yang, H. Lu, Effects of dichlorobenzene, toluene, benzene and formaldehyde chemicals on Drosophila melanogaster mortality, Environ. Geochem. Health 47 (1) (2025) 28, https://doi.org/10.1007/s10653-024-02341-4.

[3] Y. Liu, Z. Long, J. Qiu, Q. Chen, A. Yang, M. Xiao, Y. Xiao, Combined effects of benzene, toluene, xylene, ethylbenzene, and styrene exposure on hearing loss mediated by oxidative stress at realistic low levels, Environ. Pollut. 363 (2024) 125149, https://doi.org/10.1016/j.envpol.2024.125149.

[4] Y. Zhang, B. Cao, H. Yin, L. Meng, W. Jin, F. Wang, A. Al-Tabbaa, Application of zeolites in permeable reactive barriers (PRBs) for in-situ groundwater remediation: a critical review, Chemosphere 308 (2022) 136290, https://doi.org/10.1016/j.chemosphere.2022.136290.

[5] R. Mahdavi Far, B. Van der Bruggen, A. Verliefde, E. Cornelissen, A review of zeolite materials used in membranes for water purification: history, applications, challenges and future trends, J. Chem. Technol. Biotechnol. 97 (3) (2022) 575–596, https://doi.org/10.1002/jctb.6963.

[6] E.C. Umejuru, T. Mashifana, V. Kandjou, M. Amani-Beni, H. Sadeghifar, M. Fayazi, N.T. Sithole, Application of zeolite based nanocomposites for wastewater remediation: evaluating newer and environmentally benign approaches, Environ. Res. 231 (2023) 116073, https://doi.org/10.1016/j.envres.2023.116073.

[7] P.T.B. Fischer, D. Di Trapani, V.A. Laudicina, A. Mineo, S.M. Muscarella, G. Mannina, Adsorption and desorption of ammonium from treated wastewater by zeolite filled columns: an experimental study at the water resource recovery facility of Palermo University–Italy, J. Environ. Manag. 375 (2025) 124241, https://doi.org/10.1016/j.jenvman.2025.124241.

[8] L. Pasti, E. Rodeghero, G. Beltrami, M. Ardit, E. Sarti, T. Chenet, C. Stevanin, A. Martucci, Insights into adsorption of chlorobenzene in high silica MFI and FAU zeolites gained from chromatographic and diffractometric techniques, Minerals 8 (3) (2018) 80, https://doi.org/10.3390/min8030080.

[9] I. Braschi, S. Blasioli, E. Buscaroli, D. Montecchio, A. Martucci, Physicochemical regeneration of high silica zeolite Y used to clean-up water polluted with sulfonamide antibiotics, J. Environ. Sci. 43 (2016) 302–312, https://doi.org/10.1016/j.jes.2015.07.017.

[10] S. Wang, H. Li, S. Xie, S. Liu, L. Xu, Physical and chemical regeneration of zeolitic adsorbents for dye removal in wastewater treatment, Chemosphere 65 (1) (2006) 82–87, https://doi.org/10.1016/j.chemosphere.2006.02.043.

[11] E. Katsou, S. Malamis, M. Tzanoudaki, K.J. Haralambous, M. Loizidou, Regeneration of natural zeolite polluted by lead and zinc in wastewater treatment systems, J. Hazard. Mater. 189 (3) (2011) 773–786, https://doi.org/10.1016/j.jhazmat.2010.12.061.

[12] D.G. Lee, J.H. Kim, C.H. Lee, Adsorption and thermal regeneration of acetone and toluene vapors in dealuminated Y-zeolite bed, Sep. Purif. Technol. 77 (3) (2011) 312–324, https://doi.org/10.1016/j.seppur.2010.12.022.

[13] M. Mancinelli, A. Martucci, G.M. Salani, G. Bianchini, L. Gigli, J.R. Plaisier, F. Colombo, High temperature behaviour of Ag-exchanged Y zeolites used for PFAS sequestration from water, Phys. Chem. Chem. Phys. 25 (29) (2023) 20066–20075, https://doi.org/10.1039/D3CP01584J.

[14] V. Daligaux, R. Richard, M.H. Manero, Deactivation and regeneration of zeolite catalysts used in pyrolysis of plastic wastes—a process and analytical review, Catalysts 11 (7) (2021) 770, https://doi.org/10.3390/catal11070770.

[15] L. Leardini, A. Martucci, I. Braschi, S. Blasioli, S. Quartieri, Regeneration of high-silica zeolites after sulfamethoxazole antibiotic adsorption: a combined in situ high-temperature synchrotron X-ray powder diffraction and thermal degradation study, Mineral. Mag. 78 (5) (2014) 1141–1159, https://doi.org/10.1180/minmag.2014.078.5.04.

[16] Z. Ma, A. Ghosh, N. Asthana, J. van Bokhoven, Visualization of structural changes during deactivation and regeneration of FAU zeolite for catalytic fast pyrolysis of lignin using NMR and electron microscopy techniques, ChemCatChem 10 (19) (2018) 4431–4437, https://doi.org/10.1002/cctc.201800670.

[17] G.N. Kalantzopoulos, D.R. Gama, D.K. Pappas, I. Dovgaliuk, U. Olsbye, P. Beato, S. Svelle, Real-time regeneration of a working zeolite monitored via operando X-ray diffraction and crystallographic imaging: how coke flees the MFI framework, Dalton Trans. 51 (44) (2022) 16845–16851, https://doi.org/10.1039/D2DT02845J.

[18] E. Gabruś, J. Nastaj, P. Tabero, T. Aleksandrzak, Experimental studies on 3A and 4A zeolite molecular sieves regeneration in TSA process: aliphatic alcohols dewatering–water desorption, Chem. Eng. J. 259 (2015) 232–242, https://doi.org/10.1016/j.cej.2014.07.108.

[19] N. Precisvalle, G. Beltrami, M. Ardit, C. Giacobbe, L. Pasti, T. Chenet, A. Martucci, Temperature-induced structural changes in acidic L-zeolite: an in situ synchrotron time-resolved powder diffraction study, J. Phys. Chem. C 127 (27) (2023) 13276–13285, https://doi.org/10.1021/acs.jpcc.3c02326.

[20] Y. Wu, P. Deng, L. Liu, J. Zhang, H. Liu, X. Gao, L. Wang, Dynamic evolution of metal structures on/in zeolites for catalysis, Chem. Soc. Rev. 54 (2025) 4745–4762, https://doi.org/10.1039/D5CS00035A.

[21] G. Cruciani, Zeolites upon heating: factors governing their thermal stability and structural changes, J. Phys. Chem. Solid. 67 (9–10) (2006) 1973–1994, https://doi.org/10.1016/j.jpcs.2006.05.057.

[22] L. Palin, R. Caliandro, D. Viterbo, M. Milanesio, Chemical selectivity in structure determination by the time dependent analysis of in situ XRPD data: a clear view of Xe thermal behavior inside a MFI zeolite, Phys. Chem. Chem. Phys. 17 (26) (2015) 17480–17493, https://doi.org/10.1039/C5CP02522B.

[23] A. Martucci, M. de Lourdes Guzman-Castillo, F. Di Renzo, F. Fajula, A. Alberti, Reversible channel deformation of zeolite omega during template degradation highlighted by in situ time-resolved synchrotron powder diffraction, Microporous Mesoporous Mater. 104 (1–3) (2007) 257–268, https://doi.org/10.1016/j.micromeso.2007.02.040.

[24] G. Beltrami, F. di Renzo, I. Parodi, A. Alberti, M. de Lourdes Guzman-Castillo, F. Fajula, A. Martucci, Thermal activation of NH4 precursor of acidic omega zeolite: a neutron and in-situ synchrotron powder diffraction combined study, Microporous Mesoporous Mater. 314 (2021) 110825, https://doi.org/10.1016/j.micromeso.2020.110825.

[25] E. Rodeghero, A. Martucci, G. Cruciani, E. Sarti, A. Cavazzini, V. Costa, L. Pasti, Detailed investigation of thermal regeneration of high-silica ZSM-5 zeolite through in situ synchrotron X-ray powder diffraction and adsorption studies, J. Phys. Chem. C 121 (33) (2017) 17958–17968, https://doi.org/10.1021/acs.jpcc.7b05090.

[26] M. Mancinelli, M. Ardit, T. Chenet, L. Pasti, A. Martucci, Desorption of humic monomers from Y zeolite: a high-temperature X-ray diffraction and thermogravimetric study, Microporous Mesoporous Mater. 379 (2024) 113270, https://doi.org/10.1016/j.micromeso.2024.113270.

[27] T. Chenet, M. Mancinelli, E. Sarti, V. Costa, C. D'Anna, A. Martucci, L. Pasti, Competitive adsorption of 4-hydroxybenzaldehyde and toluene onto high silica zeolites, Environ. Proc. 11 (3) (2024) 49, https://doi.org/10.1007/s40710-024-00726-2.

[28] M. Milanesio, G. Artioli, A.F. Gualtieri, L. Palin, C. Lamberti, Template burning inside TS-1 and Fe-MFI molecular sieves: an in situ XRPD study, J. Am. Chem. Soc. 125 (47) (2003) 14549–14558, https://doi.org/10.1021/ja037229+.

[29] X. Du, X. Li, H. Zhang, X. Gao, Kinetics study and analysis of zeolite Y destruction, Chin. J. Catal. 37 (2) (2016) 316–323, https://doi.org/10.1016/S1872-2067(15)60975-5.

[30] D.S. Bhange, N.A. Pandya, R.K. Jha, V. Ramaswamy, Non-isothermal kinetic studies of the template decomposition from silicalite-1 framework—high temperature X-ray diffraction and thermogravimetric analysis, Microporous Mesoporous Mater. 113 (1–3) (2008) 64–71, https://doi.org/10.1016/j.micromeso.2007.11.002.

[31] Y. Sarıkaya, M. Önal, A.D. Pekdemir, Kinetic and thermodynamic approaches on thermal degradation of sepiolite crystal using XRD-analysis, J. Therm. Anal. Calorim. 140 (6) (2020) 2667–2672, https://doi.org/10.1007/s10973-019-09053-3.

[32] R. Snellings, G. Mertens, S. Hertsens, J. Elsen, The zeolite–lime pozzolanic reaction: reaction kinetics and products by in situ synchrotron X-ray powder diffraction, Microporous Mesoporous Mater. 126 (1–2) (2009) 40–49, https://doi.org/10.1016/j.micromeso.2009.05.017.

[33] M.L. Gualtieri, A.F. Gualtieri, J. Hedlund, The influence of heating rate on template removal in silicalite-1: an in situ HT-XRPD study, Microporous Mesoporous Mater. 89 (1–3) (2006) 1–8, https://doi.org/10.1016/j.micromeso.2005.09.022.

[34] N. Sbirrazzuoli, Model-free isothermal and nonisothermal predictions using advanced isoconversional methods, Thermochim. Acta 697 (2021) 178855, https://doi.org/10.1016/j.tca.2020.178855.

[35] S. Vyazovkin, S. Vyazovkin, Isoconversional methodology, in: Isoconversional Kinetics of Thermally Stimulated Processes, 2015, pp. 27–62.

[36] A. Mianowski, M. Sciazko, T. Radko, Vyazovkin's isoconversional method as a universal approach, Thermochim. Acta 696 (2021) 178822, https://doi.org/10.1016/j.tca.2020.178822.

[37] P. Budrugeac, Applicability of model-free isothermal prediction procedures based on the Friedman method and three incremental isoconversional methods for complex processes, Thermochim. Acta 733 (2024) 179691, https://doi.org/10.1016/j.tca.2024.179691.

[38] I. Braschi, S. Blasioli, L. Gigli, C.E. Gessa, A. Alberti, A. Martucci, Removal of sulfonamide antibiotics from water: evidence of adsorption into an organophilic zeolite Y by its structural modifications, J. Hazard. Mater. 178 (1–3) (2010) 218–225, https://doi.org/10.1016/j.jhazmat.2010.01.066.

[39] I. Braschi, G. Gatti, G. Paul, C.E. Gessa, M. Cossi, L. Marchese, Sulfonamide antibiotics embedded in high silica zeolite Y: a combined experimental and theoretical study of host–guest and guest–guest interactions, Langmuir 26 (12) (2010) 9524–9532, https://doi.org/10.1021/la9049132.

[40] J.D. Hancock, J.H. Sharp, Method of comparing solid-state kinetic data and its application to the decomposition of kaolinite, brucite, and $BaCO_3$, J. Am. Ceram. Soc. 55 (2) (1972) 74–77, https://doi.org/10.1111/j.1151-2916.1972.tb11213.x.

[41] K.O. Strømme, On the application of the Avrami-Erofeev equation in non-isothermal reaction kinetics, Thermochim. Acta 97 (1986) 363–368, https://doi.org/10.1016/0040-6031(86)87040-X.

[42] H.P. Klug, L.E. Alexander, X-ray Diffraction Procedures: for Polycrystalline and Amorphous Materials, second ed., Wiley-Interscience, New York, 1974, p. 992.

[43] C. Weidenthaler, Pitfalls in the characterization of nanoporous and nanosized materials, Nanoscale 3 (3) (2011) 792–810, https://doi.org/10.1039/C0NR00561D.

[44] G. Sastre, J.A. Vidal-Moya, T. Blasco, J. Rius, J.L. Jordá, M.T. Navarro, F. Rey, A. Corma, Preferential location of Ge atoms in polymorph C of beta zeolite (ITQ-17) and their structure-directing effect: a computational, XRD, and NMR

spectroscopic study, Angew. Chem. Int. Ed. 41 (24) (2002) 4916–4919, https://doi.org/10.1002/anie.200290028.
[45] M. Gussoni, M. Rui, G. Zerbi, Electronic and relaxation contribution to linear molecular polarizability. An analysis of the experimental values, J. Mol. Struct. 447 (3) (1998) 163–215, https://doi.org/10.1016/S0022-2860(97)00292-5.
[46] J.R. Gascooke, E.A. Virgo, W.D. Lawrance, Direct observation of methyl rotor and vib-rotor states of S_0 toluene: a revised torsional barrier due to torsion-vibration coupling, J. Chem. Phys. 142 (2) (2015) 024315, https://doi.org/10.1039/C7SC05309F.
[47] P.J. Stephens, F.J. Devlin, C.F. Chabalowski, M.J. Frisch, Ab initio calculations of vibrational absorption and circular dichroism spectra and comparison with experiment, J. Chem. Phys. 98 (12) (1994) 11623–11627, https://doi.org/10.1021/j100096a001.
[48] W. Müller-Warmuth, R. Schüler, M. Prager, A. Kollmar, A nuclear relaxation and neutron scattering study of the rotational states of methyl groups in solids with low hindering barriers, J. Magn. Reson. 34 (1) (1979) 83–95, https://doi.org/10.1016/0022-2364(79)90031-3.
[49] J. Arcenegui-Troya, P.E. Sánchez-Jiménez, A. Perejón, L.A. Pérez-Maqueda, Determination of the activation energy under isothermal conditions: revisited, J. Therm. Anal. Calorim. 148 (4) (2023) 1679–1686, https://doi.org/10.1007/s10973-022-11728-3.
[50] J. Arcenegui-Troya, P.E. Sánchez-Jiménez, M. del Rocío Rodríguez-Laguna, A. Perejón, L.A. Pérez-Maqueda, A generalized interface reaction kinetic model for describing heterogeneous processes driven by contracting mechanisms, J. Therm. Anal. Calorim. 149 (6) (2024) 2653–2663, https://doi.org/10.1007/s10973-023-12835-5.
[51] P.E. Sánchez-Jiménez, A. Perejón, J. Arcenegui-Troya, L.A. Pérez-Maqueda, Predictions of polymer thermal degradation: relevance of selecting the proper kinetic model, J. Therm. Anal. Calorim. (2021) 1–7, https://doi.org/10.1007/s10973-021-10649-x.